ACS Sustainable Chemistry & Engineering

pubs.acs.org/journal/ascecg

Research Article

New Insights into Silicon Purification by Alloying–Leaching Refining: A Comparative Study of Mg–Si, Ca–Si, and Ca–Mg–Si Systems

Mengyi Zhu,* Sheng Ying Yue,* Kai Tang, and Jafar Safarian

Cite This: https://dx.doi.org/10.1021/acssuschemeng.0c05564

Read Online

ACCESS | Metrics & More | Article Recommendations

ABSTRACT: In the present work, a comparative study of the silicon alloying–leaching purification process was carried out on the recently developed Mg–Si system, the Ca–Si system, and the novel ternary Ca–Mg–Si system. Insights were provided into the integrated process from aspects of thermodynamic assessment, microstructural analysis, experimental observation, computational simulation, and analytical modeling. The main silicide precipitates of the three Mg–Si, Ca–Si, and Ca–Mg–Si alloys studied were determined as Mg_2Si, $CaSi_2$, and ternary $Ca_7Mg_{7.5\pm\delta}Si_{14}$, respectively. Other metallic impurities were found to form complex silicides embedded inside the main precipitate, where P also segregated and precipitated according to the interaction with the alloying elements. All of the impurities were further carried away with the removal of the main precipitates through the subsequent leaching process. It was found that the ternary Ca–Mg–Si alloy exhibits a cleaner leaching process due to the unique crystal structure of $Ca_7Mg_{7.5\pm\delta}Si_{14}$. A novel cracking–shrinking principle-based kinetics model was developed to further describe the impurity removal process. The segregation behavior of P was also modeled through a thermodynamic approach and Ca was found to have stronger P affinity compared to Mg. It was finally concluded that the novel Ca–Mg–Si ternary alloy system exhibited better performance overall as compared to the other two binary alloys.

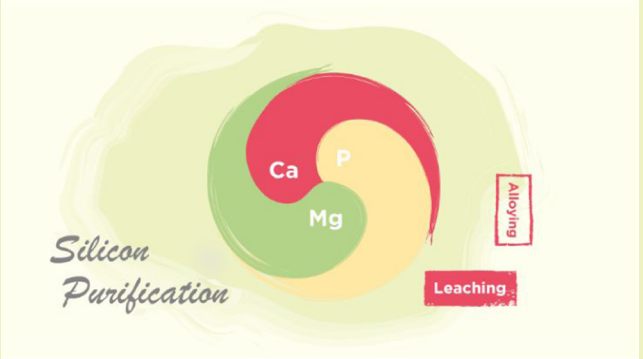

KEYWORDS: *metallurgical-grade silicon, impurities, silicide, purification, acid leaching, kinetics*

INTRODUCTION

The contribution of solar energy to the world's total energy supply has grown significantly in the past two decades. With the rapid photovoltaic market growth and installation of Si-based solar modules worldwide, it has become increasingly critical to develop an environmentally friendly approach for solar-grade silicon (SoG-Si) production.[1] Owing to the low energy consumption and low carbon footprint features, the emerging metallurgical route of SoG-Si production has received increasing attention.[1−3] As one of the recent successfully commercialized processes, the Elkem Solar process, which is operated by REC Solar Norway, is known to purify crude metallurgical-grade Si (MG-Si) through the combination of a series of metallurgical methods of slag refining, acid leaching, and direction solidification. The goal of acid leaching among these methods is to separate nonmetallic impurity P, which is one of the essential impurities in MG-Si needed to meet the strict SoG-Si impurity requirement, and also to remove the majority of metallic impurities at the same time.

The principle of acid leaching is mainly based on the digestion of segregated impurities from silicon grains during Si solidification. Impurities with lower segregation coefficients will precipitate more in the last formed solid phases (precipitates) in solidification due to their strong tendency to stay in the liquid phase. By exposing the solidified silicon to the acid solution, impurities located at grain boundaries of precipitates between the primary silicon grains can be carried away, and pure Si can be obtained. Considerable research has been performed to study the impurity extraction from MG-Si by acid leaching.[4−12] It has been found that most of the metallic impurities can be effectively extracted by adjusting a variety of processing parameters like leaching temperature, time, acid combination, and particle size, but the effective P extraction by direct leaching of MG-Si still remains a challenge. Even though it has been theoretically and experimentally confirmed that P tends to segregate along Si grain boundaries,[13] its segregation coefficient (k_p = 0.35) is still

Received: July 31, 2020
Revised: September 22, 2020

Table 1. Impurity Concentrations (ppmw) of the Produced Ca- and Mg-Doped Silicon Alloys

sample	P	Mg	Ca	Al	Fe	Ti	Mn
Mg−Si	5.39	47 022.93	125.10	785.54	1213.10	85.93	23.17
Ca−Mg−Si	5.76	24 549.51	20 847.08	919.85	1264.52	108.04	27.81
Ca−Si	4.64	7.17	35 807.49	845.79	1191.27	94.35	23.49

relatively high compared to metallic impurities, which is usually less than 10^{-3}. To further improve the extraction efficiency of P and other impurities, considerable attention has been paid to redistribute impurities by adding alloying elements as impurity getters such as calcium (Ca),[14−18] magnesium (Mg),[19−23] titanium (Ti),[17] aluminum (Al),[24−29] copper (Cu),[30−33] tin (Sn),[34,35] iron (Fe),[36−38] and nickel (Ni).[39] The widely known solvent refining usually involves alloying by Al, Sn, Cu, and Fe with a large amount of metal addition (around or more than 50 wt %). The low-temperature operation and high impurity removal degree features make the solvent-refining process promising. However, the industrialization process is hampered by the concerns of the potentially high production cost and low Si productivity caused by the need for large metal addition. From this perspective, small alloying metal addition has a better cost-effective feature, but this requires a distinctly strong impurity-gathering ability of the alloying elements.

Alkaline-earth metals are known for their strong affinity to P. Thus, metals in this group are of increasing interest for P removal from MG-Si. Anders[14] doped Ca into MG-Si and found that pure Si can be obtained after acid leaching. Shimpo et al.[15] measured the interaction coefficient of Ca and P in the Ca−Si−P system and observed the formation of Ca_3P_2 along the Si grain boundary. It was also reported that efficient P removal could be achieved by altering the Ca alloying concentration, cooling rate, and leaching conditions.[16−18] Mg is a relatively new alloying impurity getter proposed by the NTNU team in recent years,[19−23] and more knowledge about Mg is needed, in particular for comparison with the Ca−Si alloying−leaching system. In addition, according to the Zintl−Klemm concept,[40] the mixing of Ca and Mg in Si may show a pronounced variation of the electronic structure compared to the binary silicide as a result of unbalanced valence electron transfer. It is believed that the segregation behavior of the impurities and also the leaching process of the Ca−Mg−Si ternary alloying system may differ for both Ca−Si and Mg−Si binary alloying systems. Hence, it is essential to study Si purification by Ca and Mg alloying together.

In this work, a comparative study of Ca−Si, Mg−Si, and Ca−Mg−Si systems is carried out experimentally and theoretically to provide essential insights into MG-Si purification for the whole integrated process including aspects of thermodynamic assessment, alloy microstructure and impurity distribution, acid leaching experiments, kinetics modeling, and purification efficiency evaluation.

METHODOLOGY

Experimental Procedure. The Si sources used in this work are commercial MG-Si (99.5% purity, P: 15 ppmw) and mixed with commercial impurity-free Si produced from the fluidized bed reactor process (FBR-Si) to minimize the influence of other minor impurities in the present study and attain a lower P impurity concentration at several ppmw levels. The MG-Si and FBR-Si mixing ratio was fixed as 40% MG-Si and 60% FBR-Si for all of the alloys. A high-purity Mg rod (99.8% purity, Alfa Aesar) and granular Ca (99% purity, Sigma-Aldrich) were employed as the alloying metal sources, and the initial charging composition of the alloys is 5.2 wt % Mg, 4.2 wt % Ca, and 2.2 wt % Ca−2.6 wt % Mg. Considering the higher volatility of Mg at high temperatures, it was doped into Si after melting, while Ca granulates were directly charged with Si before heating. Thus, about 400 g of Si and Ca granules were first put in a high-density isotropic graphite crucible (inner diameter: 70 mm, height: 150 mm). The crucible was further heated in an induction furnace under a high-purity Ar flow (99.9999% purity) with the chamber pressure maintained at around 1030−1050 mbar. After the samples were fully melted at around 1500 °C, metallic Mg pieces were doped into the molten alloy to form the target Ca−Mg−Si and Mg−Si alloys. The molten alloys were then homogenized through induction stirring for 10 min and cooled down to room temperature. The cooling rate was kept at 20−30 °C/min as faster cooling may suppress impurity segregation, and slower cooling may lead to higher evaporation loss of the volatile alkaline-earth alloying metals. The final composition of obtained bulk alloys is listed in Table 1.

The obtained bulk alloys were crushed by a ring mill (Retsch Vibratory Disc Mill RS200, tungsten carbide sets) into fine particles within the specific particle size range from 0.2 to 1 mm before leaching. Acid leaching was performed by mixing 20 g of particles with 120 mL of reagent-grade 10% HCl (VMR International) in a beaker on a magnetic stirring hot plate, the stirring speed was fixed at 200 rpm, and the leaching temperature was fixed at 60 °C throughout the whole leaching period. Samples were taken at specific leaching times (5, 10, 20, 60, and 180 min). After 3 h leaching, samples were further cleaned by deionized water and ethanol.

The microstructure of the obtained alloys was studied by an electron probe micro-analyzer (EPMA, JXA-8500F) and the precipitate composition was measured by wavelength-dispersive spectroscopy (WDS). The impurity contents were measured by high-resolution inductively coupled plasma mass spectrometry (ICP-MS, Agilent 8800). The particle size distribution (PSD) was measured by a Horiba LA-960 instrument with the laser diffraction method. The refractive index value of pure Si is adopted for the analyzed Si-rich alloy samples as an approximation since the real value remains unknown but should reasonably be close to the value of pure Si. The particle size measurement range of the instrument is 10 nm to 5 mm. It is also worth noting that the particle size measured by laser diffraction is usually larger than the sieving particle size, as it is the diameter of a sphere with the particle's equivalent volume and the sieving particle size is the minimum diameter passing through the sieve aperture.

Computational Methods. The structural and electronic properties of the main precipitate compounds studied, Mg_2Si, $CaSi_2$, and $Ca_7Mg_{7.5\pm\delta}Si_{14}$, are investigated based on density functional theory (DFT) calculations. The crystal structures were fully optimized with the DFT simulation employing the Vienna ab initio simulation package (VASP).[41,42] The projector-augmented wave (PAW) method[43,44] for the pseudopotential, and generalized gradient approximation (GGA) with the Perdew−Burke−Ernzerhof (PBE) exchange−correlation functional are adopted.[45] The van der Waals (vdW)-corrected

https://dx.doi.org/10.1021/acssuschemeng.0c05564
ACS Sustainable Chem. Eng. XXXX, XXX, XXX−XXX

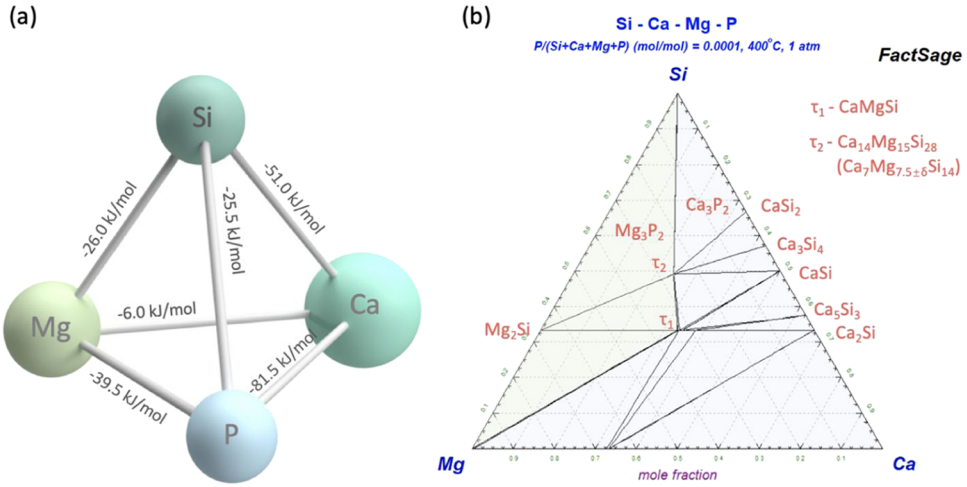

Figure 1. (a) Heat of mixing among the key elements pair in the Si−Ca−Mg−P alloy system shown with the relative atomic radius difference. (b) Modified isothermal section phase diagram of the Si−Ca−Mg−P system with 100 ppm P calculated by Factsage, where the left side shadowed region denotes Mg_3P_2 precipitation and the right-side shadowed region denotes Ca_3P_2 precipitation.

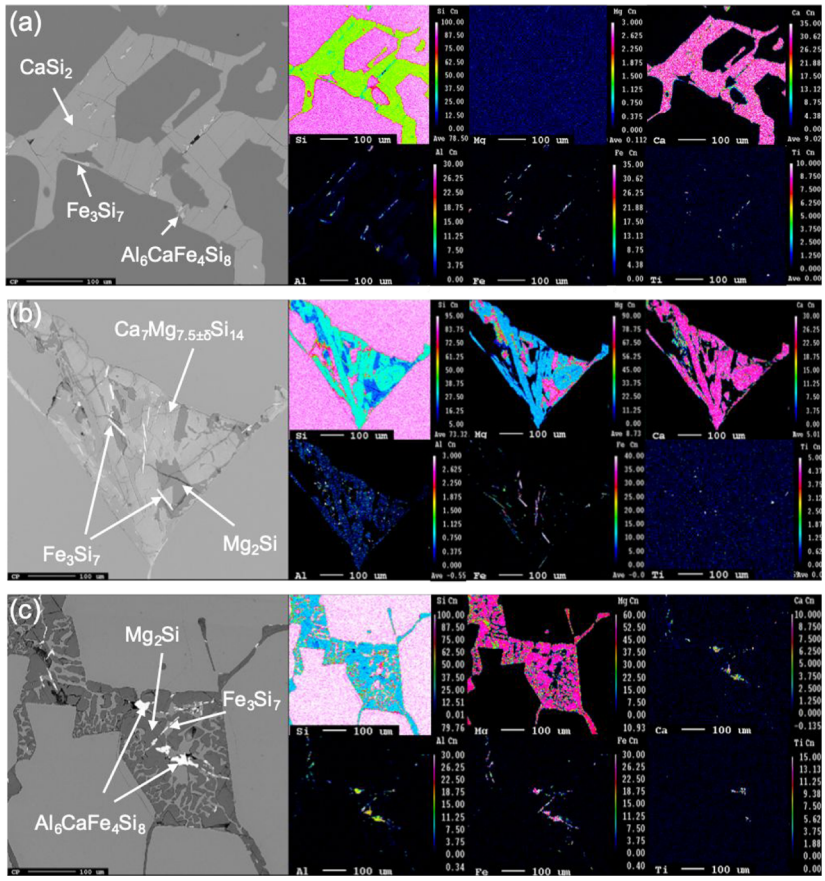

Figure 2. EPMA elemental mapping of the Ca−Si, Ca−Mg−Si, and Mg−Si alloying systems.

optB86b-vdW functional[46,47] was used throughout all of the calculations. The energy cutoff of the plane wave for the pseudopotential was 520 eV for all crystals. The γ-centered k meshes 6 × 6 × 2 were taken for $Ca_7Mg_{7.5\pm\delta}Si_{14}$. The k mesh density and the energy cutoff of augmented plane waves were checked to ensure convergence. The Hellmann−Feynman force tolerance 0.0001 eV/Å was used in all of the optimizations for structures. For the DFT calculations of $Ca_7Mg_{7.5\pm\delta}Si_{14}$, the virtual crystal approximation (VCA) method[48] was adopted employing VASP.

RESULTS AND DISCUSSION

Assessment of the Si−Ca−Mg−P System. Alkaline-earth metals are known for their strong potential to form stable phosphides as M_3P_2, where M denotes a metal.[49] Hints of the strong P affinity of Ca and Mg can also be obtained from the mixing enthalpy calculation via the Miedema model,[50] which

https://dx.doi.org/10.1021/acssuschemeng.0c05564
ACS Sustainable Chem. Eng. XXXX, XXX, XXX−XXX

Table 2. Measured Composition of Major Impurities in Alloyed MG-Si by WDS

		composition (atom %)					
sample	phase	Si	Mg	Ca	Al	Fe	Ti
Ca−Si	$CaSi_2$	65.91	0.01	33.81	0.24	0.02	0.00
	$CaAl_2Si_2$	40.03	0.30	19.79	39.74	0.13	0.01
	$Al_6CaFe_4Si_8$	43.83	0.09	6.93	28.99	20.14	0.02
	Fe_3Si_7	69.01	0.44	0.77	0.70	29.09	0.00
	$TiFeSi_2$	50.66	0.00	1.43	1.25	23.83	22.83
Ca−Mg−Si	$Ca_7Mg_{7.5\pm\delta}Si_{14}$	48.15	26.52	24.13	1.16	0.03	0.00
	Mg_2Si	34.61	65.05	0.17	0.11	0.06	0.00
	Fe_3Si_7	69.94	0.74	0.50	0.47	28.35	0.00
	$TiFeSi_2$	50.78	4.83	1.90	0.42	22.09	19.97
Mg−Si	Mg_2Si	34.51	65.21	0.01	0.23	0.03	0.00
	$Al_6CaFe_4Si_8$	42.78	3.18	5.25	29.04	19.74	0.01
	Fe_3Si_7	70.87	1.18	0.41	0.46	27.09	0.00
	$TiFeSi_2$	50.82	0.93	0.21	1.25	23.91	22.89

provides a semiempirical thermodynamic insight into the cohesion state of atoms. As the calculated results presented in Figure 1a show, the Ca−P and Mg−P pair interactions have the most negative values in the Ca−Si−P and Mg−Si−P subsystems, respectively, which implies the effectiveness of enhanced P extraction employing Ca and Mg as impurity getters. In addition, the negative values of the Ca−Mg−Si subsystems also indicate the formation of the ternary intermetallic of the Ca−Mg−Si alloy system.

To further reassess the phase equilibria of the Ca−Mg−Si−P system, a quaternary phase diagram was constructed using the commercial software Factsage using a reassessed database, as shown in Figure 1b. In the Si-rich corner, P is predicted to exist in the form of Ca_3P_2 and Mg_3P_2, mainly depending on the alloying concentration. In the Mg−Si alloy system, it is seen that only one intermetallic exists in the binary Mg−Si system, where Mg and Si form a eutectic Mg_2Si phase at 57.31 atom % Si. The eutectic temperature is 930 °C, and the Mg_2Si phase melts at temperatures above 1085 °C. The Ca−Si system becomes much more complicated when five Ca-based silicides exist, which also indicates the strong interaction between Ca and Si with each other in the melt and during solidification. In the Si-rich portion, $CaSi_2$ is the only available binary compound in the alloying−leaching approach that is known to form at 1023 °C with a eutectic point at 69.4 atom % Si. Two ternary compounds (τ_1 and τ_2) exist in the Ca−Mg−Si system, according to the study by Gröbner et al.[51] The exact stoichiometry remains controversial for the τ_2 phase as several stoichiometries ($Ca_7Mg_6Si_{14}$,[51,52] $Ca_7Mg_{7.5\pm\delta}Si_{14}$,[53] and $Ca_7Mg_{7.25}Si_{14}$[54]) have been used. Nesper et al.[53] obtained the stoichiometry of $Ca_7Mg_{7.6}Si_{14}$ from single-crystal diffraction measurements, but their simulation yields a composition of $Ca_7Mg_{7.25}Si_{14}$. Thus, the correct stoichiometry is adopted as $Ca_7Mg_{7.5\pm\delta}Si_{14}$, where δ is a measure of insecurity from the X-ray refinement. In our work, the WDS-EPMA measurement also suggests a stoichiometry of $Ca_7Mg_{7.6}Si_{14}$, but both the compositions $Ca_7Mg_6Si_{14}$ and $Ca_7Mg_{7.25}Si_{14}$ lead to a stable crystal structure from DFT calculations. Thus, the stoichiometry of the τ_2 phase presented in our work is still recommended as $Ca_7Mg_{7.5\pm\delta}Si_{14}$.

Microstructure and Impurity Redistribution. Microstructural analysis is crucial for understanding the impurity distribution during the solidification of a silicon alloy. EPMA elemental mapping was conducted for the microstructure of the studied Mg−Si, Ca−Si, and Ca−Mg−Si alloys; the results are presented in Figure 2.

The microstructure of the utilized raw MG-Si has been studied in the authors' previous work,[21−23] where only fine and dispersed Fe-bearing phases were observed in the silicon grains. However, in the alloyed MG-Si, the main precipitates were found to be strongly dependent on the alloying metals and with a thickness of around 100−200 μm after furnace cooling. The detailed compositions of the observed phases are given in Table 2. In the Ca−Si sample, the dominant precipitate phase is observed to be $CaSi_2$, with a small amount of other diversely distributed phases, such as $Al_6CaFe_4Si_8$ and Fe_3Si_7 (known as high-temperature $FeSi_2$, also called $FeSi_{2.4}$ or α-leboite),[55] as well as surrounded by some minor quantity of $CaAl_2Si_2$. Ti impurity was found to only form the ternary $TiFeSi_2$ phase, and no binary $TiSi_2$ phase was observed due to the larger amount of Fe impurity. In the Mg−Si sample, Mg_2Si is found as the main precipitate, and with a typical eutectic morphology, while other Fe-bearing phases like $Al_6CaFe_4Si_8$, Fe_3Si_7, and $TiFeSi_2$ were found embedded inside.

In the Ca−Mg−Si sample, the $Ca_7Mg_{7.5\pm\delta}Si_{14}$ ternary phase was observed as the main precipitate, and a small amount of the Mg_2Si phase was also found to coexist in the sample due to a slight Mg excess. It is also worth noting that the Al impurity found is more like to stay as a solid solution in the $Ca_7Mg_{7.5\pm\delta}Si_{14}$ phase (~1 atom %) rather than forming specific precipitates like the $CaAl_2Si_2$ and $Al_6CaFe_4Si_8$ phases in Ca−Si and Mg−Si alloys. It is also seen that Fe_3Si_7 and $FeTiSi_2$ were found to be the common phases among the Mg−Si, Ca−Si, and Ca−Mg−Si alloys, which may imply the partial substitution effect of transition metals during the solidification of Si.

The evolution of impurity redistribution was further determined by equilibrium computation by Factsage using a reassessed database shown in Figure 3. Since the temperature effect caused by the recalescence of the small amount of precipitates can be ignored, the impurity solidification sequence can be subsequently examined as well. It is seen that the primary Si is always the first nucleate phase, followed by a series of eutectic reactions that take place in the temperature range between 800 and 1000 °C, while the remaining liquid phase percentage is around 10%. The calculated main precipitates ($CaSi_2$, $Ca_7Mg_{7.5\pm\delta}Si_{14}$, Mg_2Si) in each sample also show good consistency with the EPMA results, and P suggested as the form of Ca_3P_2 and Mg_3P_2, which is dependent on the doping metal concentration. However, since their amounts are too little to detect, this cannot be confirmed by the EPMA results in this work. The Fe-bearing phases are calculated as the first

https://dx.doi.org/10.1021/acssuschemeng.0c05564
ACS Sustainable Chem. Eng. XXXX, XXX, XXX−XXX

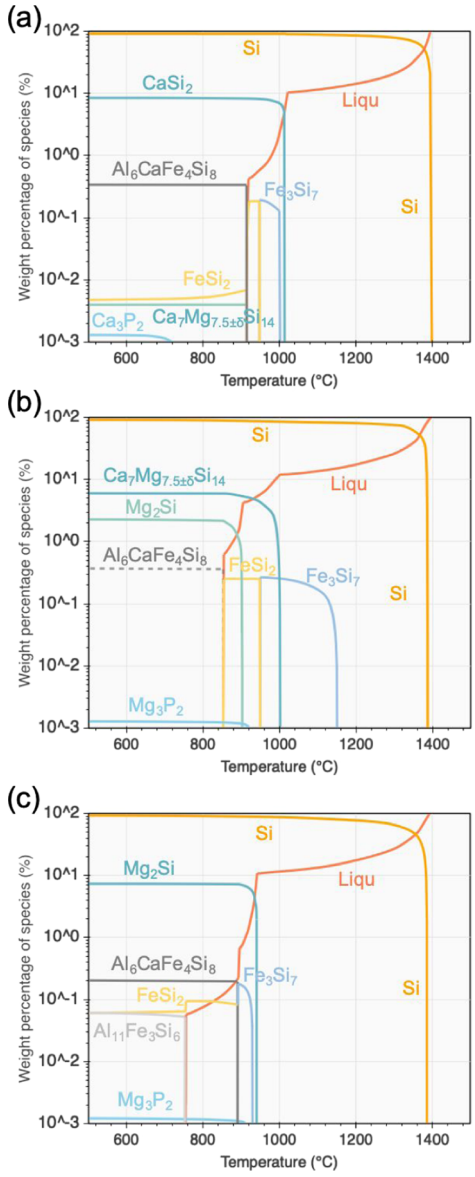

Figure 3. Calculated precipitated phase fraction and solidification sequence with the composition of studied alloys (a) Ca−Si, (b) Ca−Mg−Si, and (c) Mg−Si.

precipitated phases of minor impurity, and undergo a solid transition from the high-temperature phase Fe_3Si_7 to the low-temperature phase $FeSi_2$ via the equilibrium

$$Fe_3Si_7 \rightarrow 3FeSi_2 + Si \quad (1)$$

Since no $FeSi_2$ phase is detected in our work, it may indicate that the decomposition kinetics is slow. Al-bearing phases are suggested to form at the end of solidification. The $CaAl_2Si_2$ phase observed in the Ca−Si alloy sample is not presented in Figure 3a, which may be owing to the following reaction[56]

$$9CaAl_2Si_2 + 4Fe_3Si_7 \rightarrow 3Al_6CaFe_4Si_8 + 6CaSi_2 + 10Si \quad (2)$$

The above reactions may also explain why the observed $CaAl_2Si_2$, $Al_6CaFe_4Si_8$, and the Fe_3Si_7 phases in the Ca−Si alloy sample are often located close to each other. Nevertheless, $Al_6CaFe_4Si_8$ precipitation was not found in the Ca−Mg−Si sample; instead, Al was found as a solid solution in the $Ca_7Mg_{7.5\pm\delta}Si_{14}$ phase. Thus, the calculated precipitation of the quaternary phase in Figure 3b is marked as a dashed line.

Leaching Phenomena and Mechanism. In the initial leaching stage of all of the studied alloys, heterogeneous exothermic reactions took place rapidly along with the formation of a large number of gas bubbles. Different leaching phenomena were observed in the studied alloys, as shown in Figure 4. In the leaching of the Ca−Si sample, a yellow-green color byproduct named siloxene was formed, which is foamy and floating over the surface. Consequently, foaming bubbles were observed on top of the solution as shown in Figure 4a. In the leaching of the Mg−Si sample, intensive sparks were observed above the solution surface. Obvious minor residue (fine solid particles) can be seen in Figure 4b. Unlike the leaching of Ca−Si and Mg−Si samples, neither viscous siloxane nor intensive sparks were observed in the leaching of the Ca−Mg−Si sample, shown in Figure 4c, which makes the leaching of the Ca−Mg−Si system a cleaner process.

Leaching Mechanism. To further understand the leaching mechanism, the crystal structure and electronic characteristics of the main precipitates were investigated. The perspective views on crystal structures, Brillouin zone shape, and the band structure of $CaSi_2$, $Ca_7Mg_{7.5\pm\delta}Si_{14}$, and Mg_2Si along [001] are presented in Figure 5a−f, respectively. The differences between the three compounds are also listed in Table 3.

The formation of the foamy siloxene and massive amounts of hydrogen is the main feature of $CaSi_2$ leaching. The total leaching reaction corresponds to

$$(CaSi_2)_n + 2n\mathrm{HCl} + xn\mathrm{H_2O} \rightarrow (Si_2H_{2-x}(OH)_x)_n + n\mathrm{CaCl_2} + xn\mathrm{H_2}\,(g) \qquad (0 \le x \le 2) \quad (3)$$

where the parameter x indicates the hydrolysis degree during the leaching process and usually equals to 1.[57] As the crystal structure of $CaSi_2$ presented in Figure 5a shows, the Ca^{2+} cations formed a planar layer and were sandwiched between the

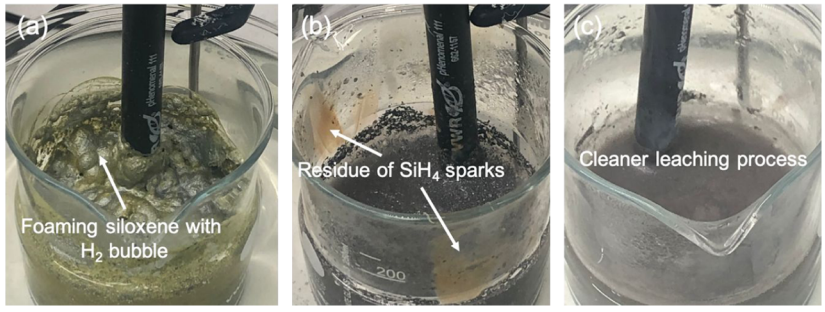

Figure 4. Top view of the solution surface after 10 min HCl leaching at 60 °C (a) Ca−Si, (b) Mg−Si, and (c) Ca−Mg−Si.

https://dx.doi.org/10.1021/acssuschemeng.0c05564
ACS Sustainable Chem. Eng. XXXX, XXX, XXX−XXX

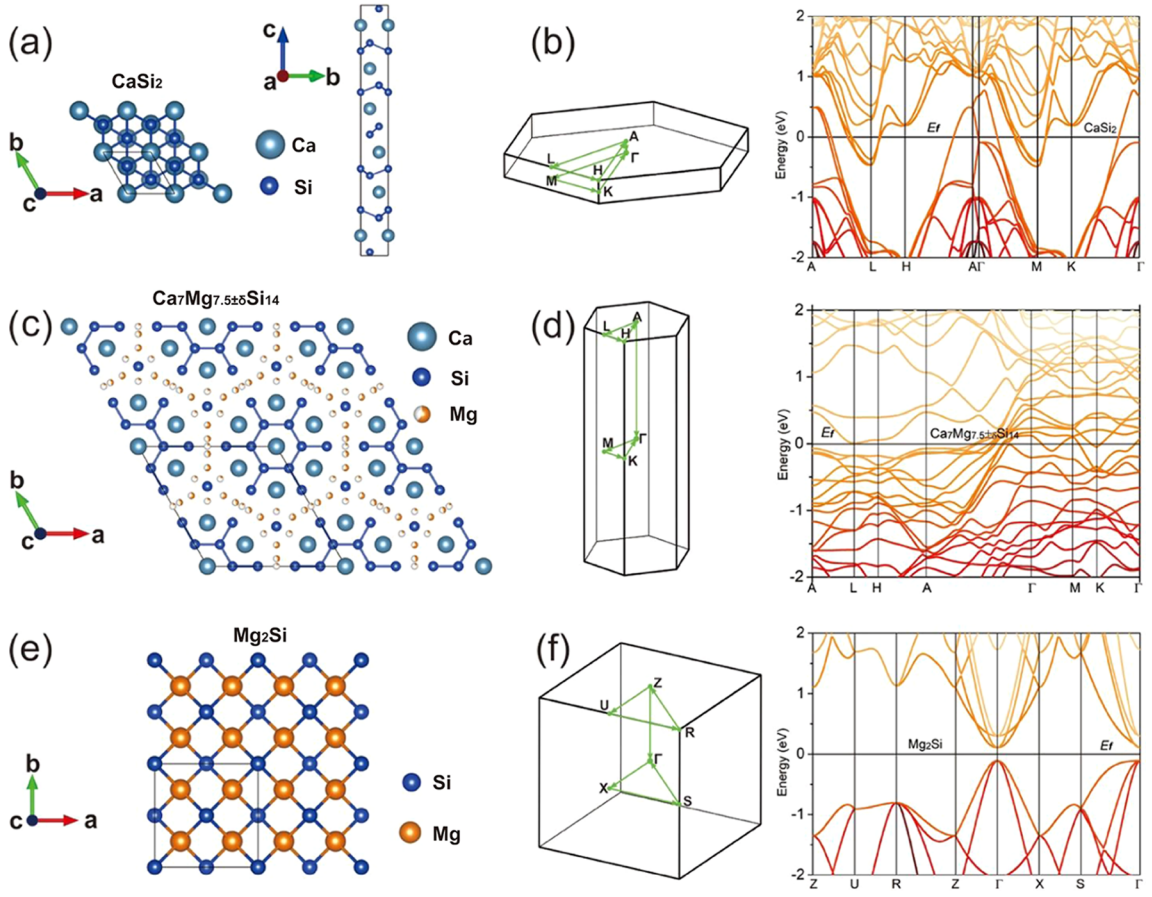

Figure 5. Crystal structure, Brillouin zone shape, and band structure of the main precipitates at the Si-rich portion in the Ca−Mg−Si system obtained by DFT calculations.

Table 3. Crystal Structure Information of the Main Precipitates of Si-rich Ca−Si, Mg−Si, and Ca−Mg−Si Alloys

compound	crystal system	space group	electrical classification
$CaSi_2$	trigonal	$R\bar{3}m$ (No.166)	metallic
Mg_2Si	cubic	$Fm\bar{3}m$ (No. 255)	semiconducting
$Ca_7Mg_{7.5\pm\delta}Si_{14}$	hexagonal	$P6/mmm$ (No.191)	metallic

corrugated Si double-anion layer. As a result, the Ca^{2+} cation layer will be replaced by the −OH and −H ions in a HCl aqueous solution, while the Si−Si bond remains unchanged. Subsequently, the siloxene forms with an intense visible luminescence, which is owing to its unique band structure.[58] The formed siloxene is water-soluble but leads to a more viscous solution and increases the difficulty of the post-cleaning procedure.

The leaching of Mg_2Si in a HCl aqueous solution is known to yield silane gas, which further combusts on exposure to air at the surface. The main reaction of Mg−Si alloy leaching is briefly written as

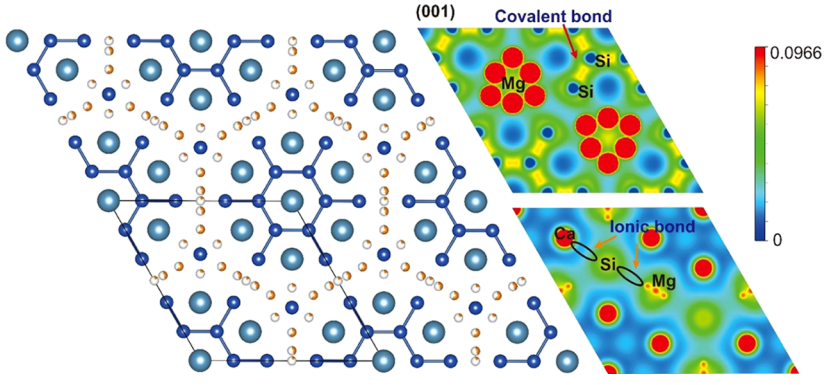

Figure 6. Charge density in the space of $Ca_7Mg_{7.5\pm\delta}Si_{14}$. The specific two-dimensional (2D)-slice projections are chosen to present the covalent and ionic bonds in $Ca_7Mg_{7.5\pm\delta}Si_{14}$. The color bar indicates the intensity of the electron charge density. The high and low values represent the positive and negative charges in space, respectively.

https://dx.doi.org/10.1021/acssuschemeng.0c05564
ACS Sustainable Chem. Eng. XXXX, XXX, XXX−XXX

$$Mg_2Si + 4HCl \rightarrow 2MgCl_2 + SiH_4(g) \quad (4)$$

As a half-silicide, Mg_2Si has a face-centered anti-CaF_2-type structure, as shown in Figure 5e, where the Mg−Si bond shows a mixed ionic and covalent nature.[59] The silane formation is thus proposed to be related to the violent breakage of the Mg−Si bonds of the isolated Si^{4-} by an acidic hydrolysis reaction. The reaction kinetics has been found to be dependent on the acid concentration in our previous work.[23] Moreover, the yield of silane gas is reported to increase with increasing temperature and acid concentration in a dilute HCl aqueous solution.[60]

The leaching mechanism of $Ca_7Mg_{7.5\pm\delta}Si_{14}$ has barely been studied so far. To the best of the authors' knowledge, only Nesper et al.[53] reported that it reacts with mineral acids with the formation of silane gas and amorphous Si. According to the experimental observations in our work, a massive gas bubble formed but with much fewer sparks compared to the leaching of the Mg−Si alloy system, and there is also no siloxene formation. Apparently, this unusual leaching behavior of $Ca_7Mg_{7.5\pm\delta}Si_{14}$ is attributed to its unique crystal structure.[53] As shown in Figure 5c, $Ca_7Mg_{7.5\pm\delta}Si_{14}$ has a highly anisotropic hexagonal crystal structure. Two types of Si atoms can be found in the unit cell: the Si_{12} planar ring type with a Ca atom in between and the isolated Si type that is coordinated by Mg atoms. The band structure obtained by DFT calculations also suggests that it is a metallic compound. Since hydrogen evolution in an acidic solution is a common phenomenon for a number of metallic silicides,[61] it is also reasonable that the generated massive gas is hydrogen. To further characterize the electronic bonding structures of $Ca_7Mg_{7.5\pm\delta}Si_{14}$, we present the atomic bonding styles via the spatial charge density in Figure 6, which is based on the jellium electron gas model. The bonding behavior of $Ca_7Mg_{7.5\pm\delta}Si_{14}$ is also strongly anisotropic with the mixing of covalent, ionic bonding features. It is also seen that in the Si_{12} planar ring, Si has a smaller charge than the isolated Si surrounded by Mg. Thus, the stoichiometry of $Ca_7Mg_{7.5\pm\delta}Si_{14}$ can also be written as $(Ca_7Mg_{7.5\pm\delta})[Si_{12}](Si_2)$.

According to the above discussion, the leaching reaction of $Ca_7Mg_{7.5\pm\delta}Si_{14}$ is, therefore, suggested to be

$$Ca_7Mg_{7.5\pm\delta}Si_{14} + (29 + 2\delta)HCl \rightarrow 7CaCl_2 + (7.5 \pm \delta)MgCl_2 + xSiH_4(g) + (14.5 - 2x)H_2(g) + (14 - x)Si \quad (0 \le x \le 7.25) \quad (5)$$

where x is close to the side of more H_2 formation and supposed to be 2 according to the stoichiometry $(Ca_7Mg_{7.5})[Si_{12}](Si_2)$.

Cracking Effect and Si Recovery. As shown in Figure 7a−c, the particle size of all studied samples decreases considerably after leaching, especially for the leaching of Ca−Si and Ca−Mg−Si samples, such that after shrinkage the size is almost half of the original size. It is apparent that strong cracking effects occurred during leaching and seem to be closely be related to the Ca concentration. By directly comparing the particle size distribution after leaching, as shown in Figure 7d, it is found that the cracking effect follows the trend Mg−Si sample < Ca−Mg−Si sample < Ca−Si sample. As a result of the cracking, the particles are more open, and accordingly, more surface is exposed to the acid solution so that it significantly accelerates the reaction progression.

Another parameter strongly related to the cracking effect is Si recovery, which is also crucial for the purification process evaluation. Its value was measured by comparing the sample weight before and after leaching, shown in Figure 8. A distinct

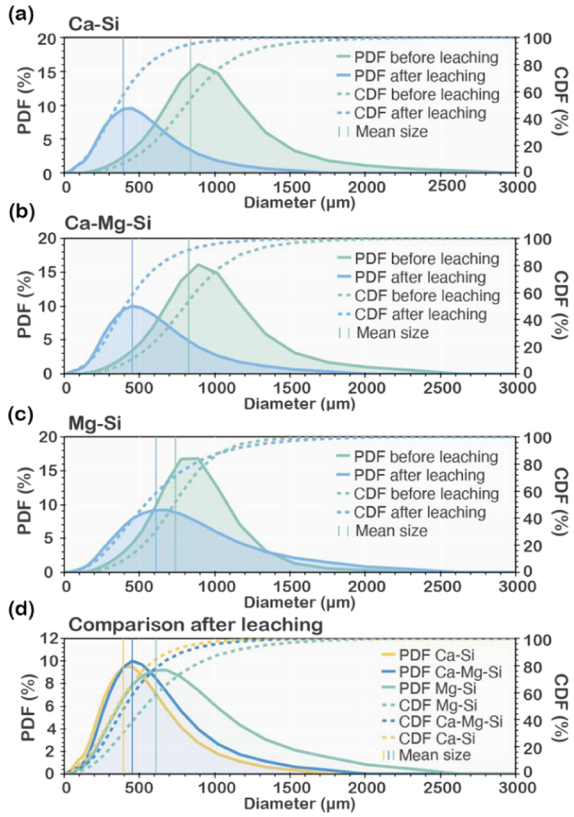

Figure 7. Particle size distribution of Si alloys before and after leaching (PDF is the probability density function, CDF is the cumulative density function): (a) Ca−Si, (b) Mg−Si, (c) Ca−Mg−Si, and (d) comparison of particle size distribution after leaching.

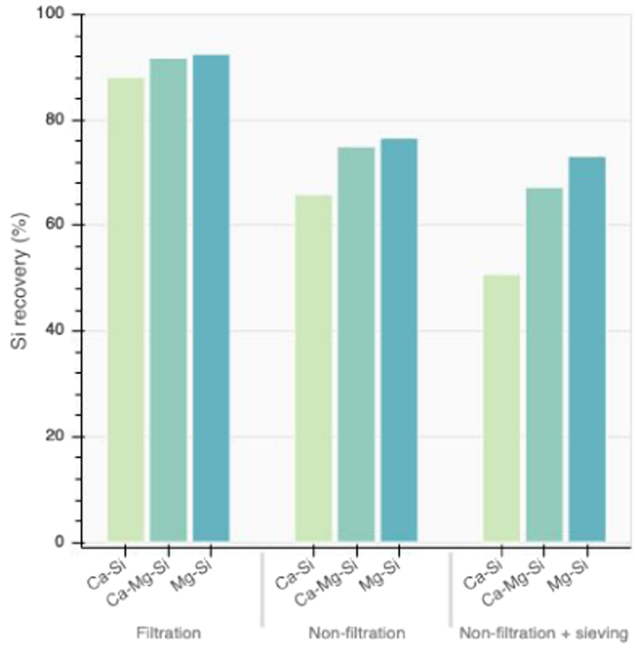

Figure 8. Comparison of Si recovery in the Ca−Si, Ca−Mg−Si, and Mg−Si systems under conditions of filtration, nonfiltration, and 0.2 mm mesh sieving after nonfiltration.

trend can be seen where the filtration method shows the highest Si recovery systematically, followed by nonfiltration (direct pouring of the solution after leaching). The nonfiltration process

https://dx.doi.org/10.1021/acssuschemeng.0c05564
ACS Sustainable Chem. Eng. XXXX, XXX, XXX−XXX

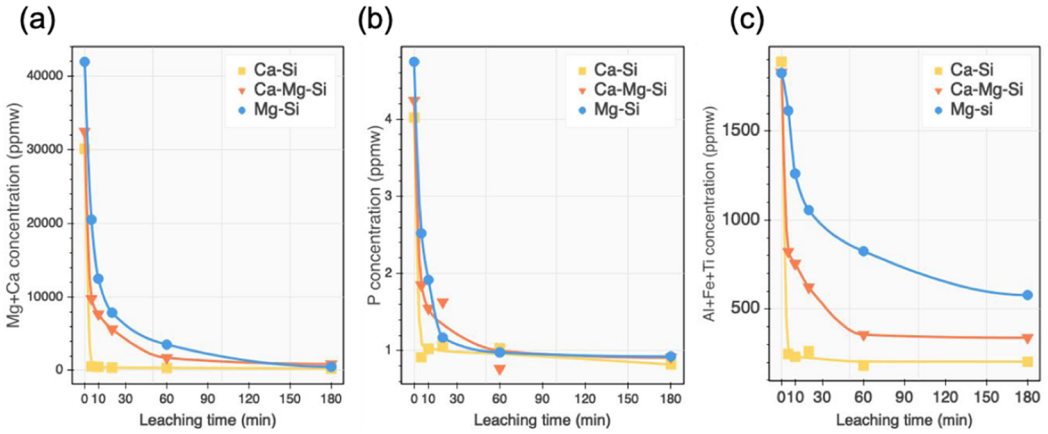

Figure 9. Effect of leaching time on the remaining impurity (a) removal of Mg + Ca, (b) removal of P, and (c) removal of Al + Fe + Ti.

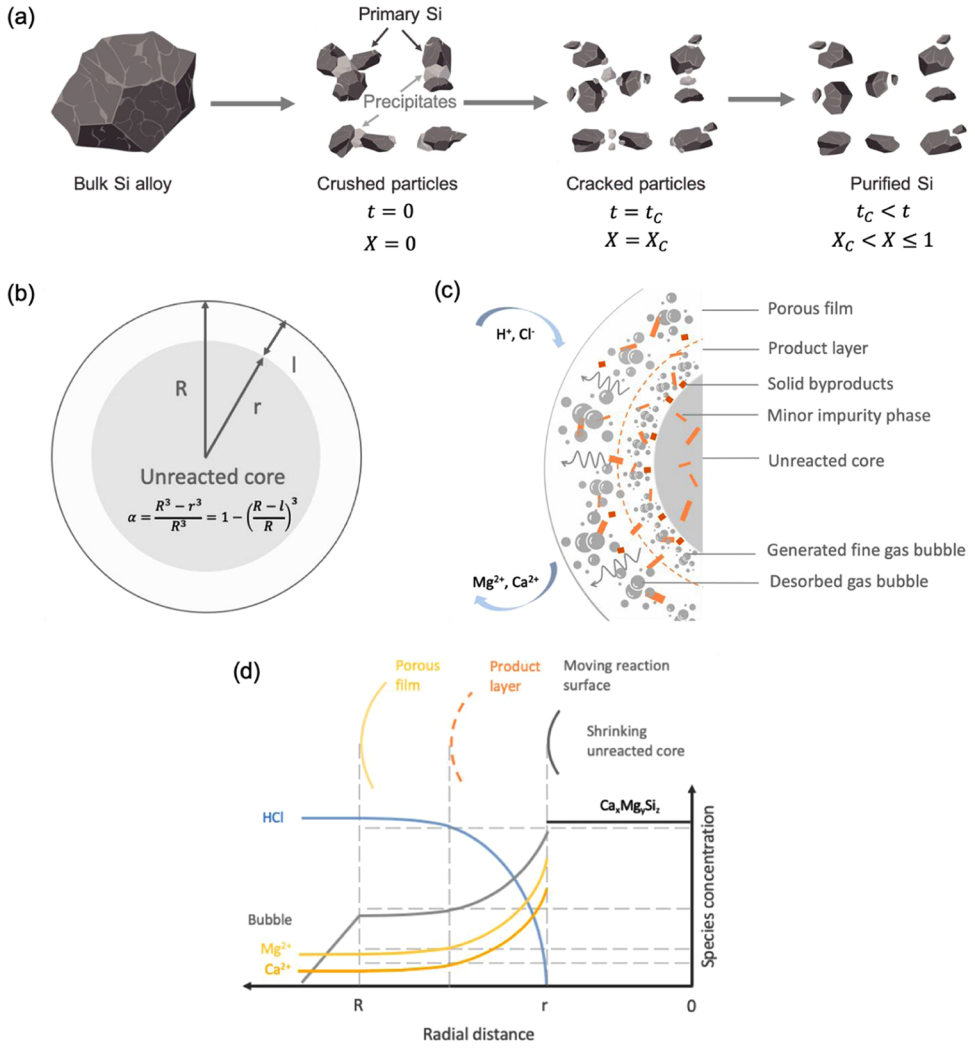

Figure 10. Illustration of the proposed cracking−shrinking model (a) representation of the entire impurity extraction process of the main stages, (b) representation of the extent of impurity conversion during the shrinking stage as a spherical particle, (c) sketch of the leaching mechanism with heterogeneous byproducts and a shrinking unreacted core, and (d) concentration profile with different radial distances.

with additional sieving obtains the least recovery, which further removes insoluble fine particles that are concentrated on the impurities. For the leached samples, the Si recovery rate exhibits the sequence Mg−Si sample > Ca−Mg−Si sample > Ca−Si sample, especially when the fine particles with a diameter smaller than 0.2 mm are sieved out. This is attributed to the increase in particle cracking with increasing Ca content, as shown in Figure 7. Consequently, the generated ultrafine particles were easily lost due to the buoyancy and hydrodynamic thrust in the post-cleaning and washing process, and most of them were sieved out after drying. Thus, the lowest recovery of Si was observed in the

https://dx.doi.org/10.1021/acssuschemeng.0c05564
ACS Sustainable Chem. Eng. XXXX, XXX, XXX−XXX

Ca−Si system, and only 50.8% purified Si was obtained from the Ca−Si alloy after sieving out the fine particles.

Leaching Kinetics. The results of the concentration measurements of the remaining impurities in the three leached alloys at different times are shown in Figure 9. It can be distinctly seen that the Ca−Si leaching displays the fastest kinetics, where most of the impurities were removed in around 10 min. Meanwhile, for the leaching of Ca−Mg−Si and Mg−Si alloys, even though for both of them the P removal shows similar efficiency, in general, impurity removal kinetics in the Ca−Mg−Si alloys is faster than that in the Mg−Si alloys, especially for the removal kinetics of Al, Fe, and Ti impurities. In fact, leaching kinetics is mainly affected by the properties of the main precipitated silicide. As shown in Figure 2, although the size of the main precipitates is similar, significant morphology differences can be observed in the Mg−Si sample. The complex two-phase eutectic pattern may impede the acid attack and suppress the cracking effect during leaching.

As one of the most important factors that affect the kinetics, the cracking of particles has been widely reported in the literature for several Si-rich alloys, such as the Fe−Si,[38,62] Ca−Si,[63] and Cu−Si[30] systems. Margarido et al.[38,64] proposed a cracking−shrinking model to describe the kinetics of Fe−Si leaching. It was also found that this model works for the leaching of the slag-treated Ca−Si alloy system as well. In the aqua regia leaching of Cu−Si briquettes by Huang et al.,[30] a modified shrinking mechanism controlled by both interfacial transfer and product layer diffusion was observed after cracking. However, in the present work, neither the mentioned models nor other commonly used and reviewed models[65] can be adopted to fit our leaching results. Thus, a novel cracking−shrinking model was developed to describe the leaching behavior of Mg−Si and Ca−Mg−Si alloys.

Modeling Assumptions. To simplify the problem, the purification process is assumed to take place in two separate stages, a leaching−cracking stage and a leaching−shrinking stage, as shown in Figure 10a. The total impurity conversion during the leaching−cracking stage is summarized as X_c. The time period of the leaching−cracking stage is set as t_c, which mainly depends on the alloy composition. More details are described below.

- Leaching−cracking stage: at $t = 0$, acid leaching starts with a total impurity conversion $X = 0$, precipitates start to be attacked by chemicals, while the microcracks keep propagating; it is worth noting that when the cracking finishes at $t = t_c$, the leaching−shrinking stage starts with the conversion $X = X_c$.
- Leaching−shrinking stage: from $t \geq t_c$, to the end of leaching, the core shrinking stage follows the kinetic model. The total impurity conversion at this stage varies as $X_c < X \leq 1$, while the impurity conversion in the shrinking stage is specifically denoted as α, which can be seen in Figure 10b, and is described later in Modeling Approach.

Figure 10c illustrates the heterogeneous reaction that occurs during the leaching−shrinking stage. A large number of gas bubbles form at the reaction surface, and particularly in the early shrinking stage. It is assumed that a product layer is formed due to the massive outspreading bubbles and also some solid byproducts. Therefore, the diffusion of acidic species is significantly limited. Meanwhile, the growing bubble also forms a bubble−liquid film, which also inhibits the diffusion process. Consequently, the concentration gradient is formed, as can be seen from Figure 10d.

Modeling Approach. In the shrinking stage, impurity conversion is defined as

$$\alpha = \frac{X - X_C}{1 - X_C} \tag{6}$$

where X is the measured impurity removal degree and α is the fraction conversion during shrinking. Considering a layer of the leachable phase around the Si grain particle (Figure 10b), the geometric relationship of the impurity removal degree can be written as

$$\alpha = \frac{R^3 - r^3}{R^3} = 1 - \left(\frac{r}{R}\right)^3 = 1 - \left(\frac{R - l}{R}\right)^3 \tag{7}$$

where R and r indicate the initial radius and unreacted radius of particles in the shrinking stage, respectively, and l indicates the thickness of the reacted eutectic phase in radial dimensions, which is a reacted shell.

Rearranging eq 7, we obtain

$$\left(\frac{R - l}{R}\right)^3 = 1 - \alpha \tag{8}$$

$$l = R[1 - (1 - \alpha)^{1/3}] \tag{9}$$

As described before, the massive erupted gas bubble actively suppresses the diffusion and reveals time-dependent characteristics. Several fluid−solid kinetic models were tested, and it was found that the product layer assumption of the Kröger−Ziegler model[65−67] fits our case. In this case, the growth rate of the product layer is inversely proportional to its thickness and time, which can be expressed as

$$\frac{dl}{dt} = \frac{k}{lt} \tag{10}$$

where k is a constant that incorporates physical and chemical parameters. However, it is known that the Kröger−Ziegler model is directly modified from the original Jander model,[68,69] where both are based on the assumption of a constant reaction surface. Nevertheless, for a shrinking particle in our case, the surface curvature should be considered since the reaction area is not constant anymore and keeps decreasing.[69−71] Thus, in the current model, the approach of the Ginstling−Brounshtein model[69−71] is introduced to describe the shrinking of spherical particles under spherical coordinates

$$\frac{dl}{dt} = \left(\frac{R}{l(R - l)}\right)\frac{k}{6t} \tag{11}$$

Integrating eq 11 by considering the boundary conditions gives

$$\int_0^l \frac{l(R - l)}{6R} dl = \int_{t_c}^t k\frac{1}{t} dt \tag{12}$$

It yields

$$l^2\left(\frac{2l}{R} - 3\right) = k \ln\left(\frac{t}{t_c}\right) \tag{13}$$

Combining eqs 9 and 13, we then obtain the following shrinking shell model equation

https://dx.doi.org/10.1021/acssuschemeng.0c05564
ACS Sustainable Chem. Eng. XXXX, XXX, XXX−XXX

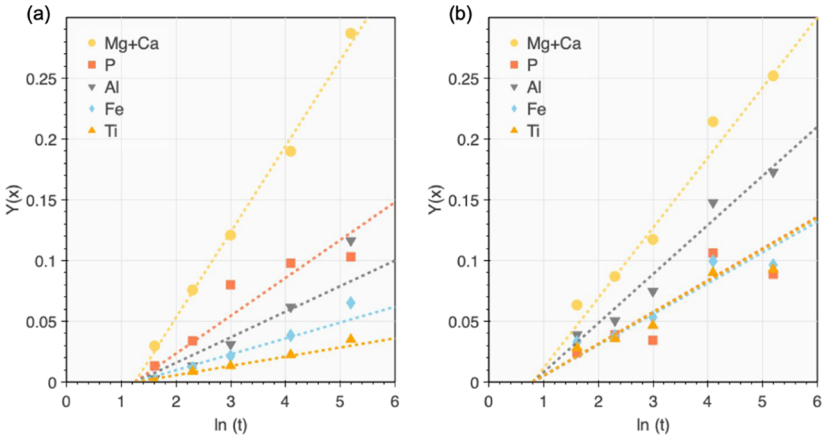

Figure 11. Application of the present cracking−shrinking shell model to the leaching of impurities with 10% HCl at 60 °C under magnetic stirring of (a) Mg−Si and (b) Ca−Mg−Si alloys.

Table 4. Obtained Fitting Parameters of Impurity Elimination from Mg−Si and Ca−Mg−Si Alloys by Leaching

	Mg−Si					Ca−Mg−Si				
impurity	ln (t_c) (min)	X_c	ξ	K_C (min^{-1})	K_S	ln (t_c) (min)	X_c	ξ	K_C (min^{-1})	K_S
Mg + Ca	1.25	0.1	1.0	0.029	0.071	0.8	0.2	1.0	0.246	0.058
P			0.8	0.023	0.031			0.6	0.147	0.026
Al			0.1	0.003	0.021			0.6	0.147	0.040
Fe			0.05	0.001	0.013			0.6	0.147	0.025
Ti			0.05	0.001	0.008			0.6	0.147	0.026

$$1 - \frac{2}{3}\alpha - (1-\alpha)^{2/3} = \frac{2k}{R^2}\ln\left(\frac{t}{t_c}\right) \qquad (t \geq t_c) \tag{14}$$

Finally, after introducing the cracking term and let $K_S = \frac{2k}{R^2}$ The model becomes

$$1 - \frac{2}{3}\left(\frac{X - X_C}{1 - X_C}\right) - \left(1 - \left(\frac{X - X_C}{1 - X_C}\right)\right)^{2/3} = K_S \ln\left(\frac{t}{t_c}\right) \qquad (t \geq t_c) \tag{15}$$

Since the conversion rate for different impurities is different, the value of X_C for each impurity should be different. For instance, the conversion of Ca and Mg was observed to be the most rapid, but the conversion of Fe and Ti was much slower. Herein, a term $\xi_i \in [0, 1]$ is introduced to evaluate the impurity i removal extent in connection with the Ca and Mg silicide conversions. Therefore, $\xi_{Mg+Ca} = 1$ is defined as the benchmark. Subsequently, the total conversion of impurities in the cracking stage can be expressed as $X_{i,c} = \xi_i X_c^{Mg+Ca}$. Hence, a more general expression of the derived kinetics model is rewritten as

$$1 - \frac{2}{3}\left(\frac{X_i - \xi_i X_c^{Mg+Ca}}{1 - \xi_i X_c^{Mg+Ca}}\right) - \left(1 - \left(\frac{X_i - \xi_i X_c^{Mg+Ca}}{1 - \xi_i X_c^{Mg+Ca}}\right)\right)^{2/3} = K_S \ln\left(\frac{t}{t_c}\right) \qquad (t \geq t_c) \tag{16}$$

It can be seen that when $t = t_c$, we have $X_i = X_{i,C} = \xi_i X_c^{Mg+Ca}$; subsequently, the term $\frac{X_i - \xi_i X_c^{Mg+Ca}}{1 - \xi_i X_c^{Mg+Ca}}$ becomes zero. If the cracking effect can be ignored as $X_c^{Mg+Ca} = 0$, the left-hand side equation is then reduced to the Ginstling−Brounshtein model. Thus, the developed model merges the features of the Ginstling−Brounshtein model and the Kröger−Ziegler model. In addition, some drawbacks in the original Kröger−Ziegler model are overcome in the present modification. For instance, the original mathematic singularity issue of the term ln(t) no longer exists. The sign paradox between $0 < t < 1$ and $1 < t$ is also avoided. Furthermore, the effect integration constant is also ruled out through definite integration in eq 12. Nevertheless, the cost of this modification is that the total rate constant is split into two parts: the cracking stage rate constant K_C and the shrinking stage rate constant K_S. As a result, the two rate constants should be considered together to compare the overall kinetics of different impurities or of different materials.

Model Evaluation. Based on the developed model above, a series of calculations were carried out to evaluate it. It is also worth noting that special modification should be applied to P prior to the calculations because of its relatively high segregation coefficient, which makes a part of P remain in Si grains and theoretically is not involved in the conversion process. Thus, the modified P conversion is expressed as

$$X_p = \frac{\eta N_{bulk} - N_t}{\eta N_{bulk}} \tag{17}$$

where N_{bulk} is the measured P concentration in bulk material and N_t is the measured P concentration at leaching time t. η is the percentage of P that segregated outside Si; ηN_{bulk} also indicates the effective concentration of P that takes part in the leaching process.

In the calculation, η is set as 0.85 approximately for both alloys based on the P segregation model in the Si alloy.[23] Since the error range is quite narrow for η, the impact on the calculation accuracy can be ignored. As shown in Figure 11, by fitting the experimental data of Mg−Si and Mg−Ca−Si alloys, a linear relationship is observed by setting $Y(X_i) = 1 - \frac{2}{3}\left(\frac{X_i - \xi_i X_c^{Mg+Ca}}{1 - \xi_i X_c^{Mg+Ca}}\right) - \left(1 - \left(\frac{X_i - \xi_i X_c^{Mg+Ca}}{1 - \xi_i X_c^{Mg+Ca}}\right)\right)^{2/3}$, and all origins from the same starting time, which is the cracking time. The

https://dx.doi.org/10.1021/acssuschemeng.0c05564
ACS Sustainable Chem. Eng. XXXX, XXX, XXX−XXX

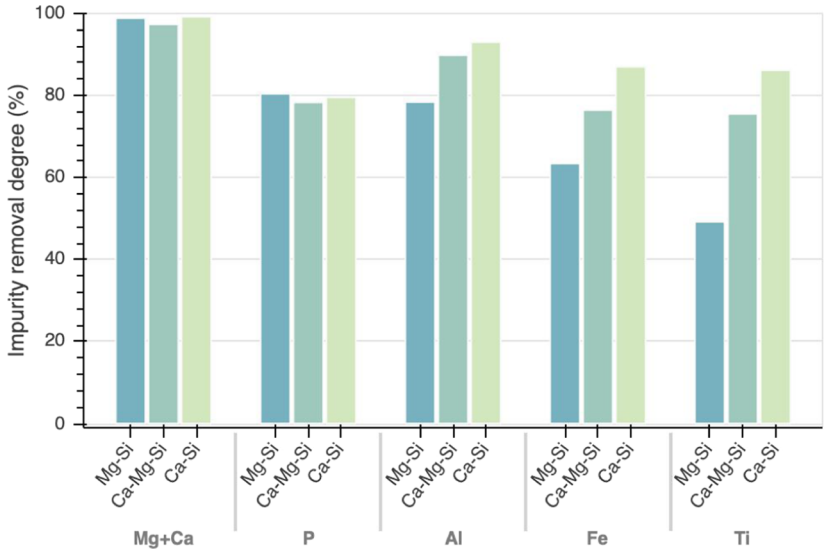

Figure 12. Comparison of impurity removal degree of the Mg−Si, Ca−Si, and Ca−Mg−Si alloying systems after 3 h acid leaching by 10% HCl at 60 °C under magnetic stirring.

fitting parameters are listed in Table 4, where K_C is calculated by $K_{i,C} = \frac{\xi_i X_c^{Mg+Ca}}{t_c}$. It can be seen from Table 4 that t_c in Mg−Si is longer than that in the Ca−Mg−Si alloy accompanied by a minor value of X_C, which reflects a more intense cracking effect for the leaching of the Ca−Mg−Si alloy.

Impurity Removal. *Overall Impurity Removal Degree.* The impurity removal degree is calculated as

$$\text{removal degree } (\%) = \frac{C_{\text{initial}} - C_{\text{final}}}{C_{\text{initial}}} \times 100 \tag{18}$$

where C_{initial} and C_{final} represent the impurity concentrations of leaching particles before and after leaching, respectively.

Ca and Mg can be nearly completely removed from all of the alloys by leaching as shown in Figure 12, while for the removal of other metallic impurities like Al, Fe, and Ti, the following order is determined: Ca−Si sample > Ca−Mg−Si sample > Mg−Si sample. The P removal degree of the investigated systems is similar and close to 80% under the applied leaching conditions. Thus, it is considered that the P removal of the three studied alloys is at an equivalent level since the differences are insignificant to distinguish, and it is necessary to consider a certain level of uncertainty when dealing with trace amounts of impurity. However, it is worth noting that this equivalent P removal degree is reached by different Ca and Mg alloying amounts. By comparing the required alloying concentration for the equivalent P removal, as presented in Figure 13, it can be seen that more Mg addition is required than Ca based on both molar and weight percentage. Consequently, with a fixed total alloying amount, the P removal efficiency from high to low should follow the trend Ca addition > Ca−Mg addition > Mg addition. Further theoretical comparison of the efficiency of alloying elements is described in the following section through thermodynamic calculations.

P Segregation Coefficient. Impurity elements are subject to solid/liquid segregation during the Si alloy solidification when the liquid alloy is solidified between the liquidus and eutectic temperatures. Knowledge of how the alloying metals affect the impurity segregation ratio is necessary to have a better understanding of the impurity removal by the alloying−leaching

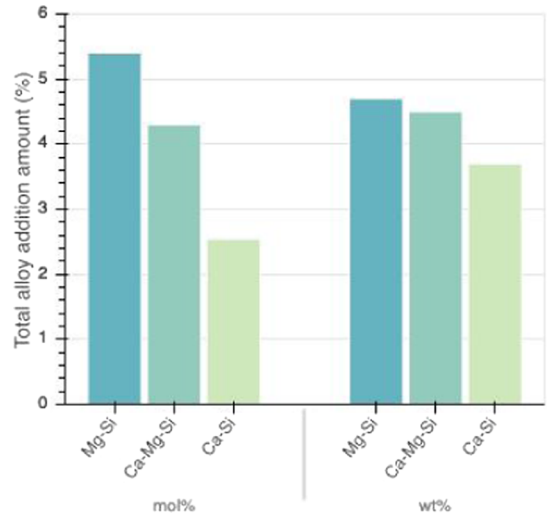

Figure 13. Comparison of required alloy addition amount for around 80% P removal.

approach. In the Ca−Mg−Si alloying system, the segregation coefficient of P between solidified Si grains and the remaining liquid can be expressed as

$$k_P^{Ca-Mg-Si} = \frac{X_{P \text{ in } Si(s)}}{X_{P \text{ in } Ca-Mg-Si(l)}} \tag{19}$$

where $X_{P \text{ in } Si(s)}$ and $X_{P \text{ in } Ca-Mg-Si(l)}$ are the P concentrations in solid primary Si and the remaining Ca−Mg−Si alloy melt, respectively, during the solidification. While the system is under an equilibrium state, the chemical potential of P in the coexisting solid and liquid phases is the same. Assuming that the dissolution energy difference of P in liquid Si and the liquid Si-rich alloy is insignificant due to the ultralow P concentration, and considering the negligible amount of metallic impurities in the solid Si, one obtains

$$\frac{X_{P \text{ in } Si(s)}}{X_{P \text{ in } Ca-Mg-Si(l)}} = \frac{\gamma_{P \text{ in } Ca-Mg-Si(l)}}{\gamma^0_{P \text{ in } Si(s)}} \tag{20}$$

https://dx.doi.org/10.1021/acssuschemeng.0c05564
ACS Sustainable Chem. Eng. XXXX, XXX, XXX−XXX

where $\gamma_{P\ in\ Ca-Mg-Si(l)}$ and $\gamma^0_{P\ in\ Si(s)}$ are the activity coefficients of P in the Ca−Mg−Si melt and in primary Si, respectively. In addition, the activity coefficient of P in the Ca−Mg−Si melt can be further reasonably written in terms of the first-order interaction coefficient terms, as expressed by Bale and Pelton[72]

$$\ln \gamma_{P\ in\ Ca-Mg-Si(l)} = \ln \gamma^0_{P\ in\ Si(l)} + \ln \gamma_{Si(l)} + \varepsilon^P_{P\ in\ Si} X_{P\ in\ Si(l)} + \varepsilon^P_{Mg\ in\ Si} X_{Mg\ in\ Si(l)} + \varepsilon^P_{Ca\ in\ Si} X_{Ca\ in\ Si(l)} \quad (21)$$

Neglecting the self-interaction term of P due to its sufficiently low content, and also $\ln \gamma_{Si(l)} \approx 0$, eq 22 can be derived by combining eqs 19 and 21

$$k_P^{Ca-Mg-Si} = \exp(\varepsilon^P_{Mg\ in\ Si} X_{Mg\ in\ Si(l)} + \varepsilon^P_{Ca\ in\ Si} X_{Ca\ in\ Si(l)}) \quad (22)$$

It can be seen that the P segregation coefficient in its dilute solutions in Si is mainly influenced by the alloyed Mg and Ca concentrations and their interaction coefficient value with P. The averaged value of $\varepsilon^P_{Mg\ in\ Si}$ during the solidification of the Mg−Si system was estimated to be −10.8 in our previous work,[23] and the value of $\varepsilon^P_{Ca\ in\ Si}$ at 1450 °C was determined to be −14.6(±1.7) according to Shimpo et al.[15] Thus, if we assume that the averaged value of $\varepsilon^P_{Ca\ in\ Si}$ during the whole solidification range is equivalent to −14.6, reasonably, it can be expected that Ca leads to more reduction of the P segregation coefficient than that of Mg with the same amount.

Figure 14 is plotted to investigate further the effect of Ca and Mg alloying on the P segregation behavior, and the isocurve of the P segregation coefficient with varying alloying concentrations is also shown as the solid lines. The P segregation coefficient is seen to decrease distinctly with increasing concentrations of Ca and Mg components. Meanwhile, it also follows the trend Ca−Si sample < Ca−Mg−Si sample < Mg−Si sample. However, since the leaching results suggest that the studied alloys show almost equivalent P removal, several reasons may be attributed to this inconsistency. First, the stronger cracking effect of the Ca−Si system may promote the P removal. Second, the averaged value of $\varepsilon^P_{Ca\ in\ Si}$ during the whole solidification range might be more negative than the measured value at 1450 °C. To investigate the effect of the interaction coefficient value, a tentative empirical value of $\varepsilon^P_{Ca\ in\ Si} = -20.0$ was also employed to calculate the isocurves as presented in Figure 13 by the dashed lines. It can be seen that a more negative interaction coefficient value fits better with the experimental results. Nevertheless, no matter which value is appropriate, it can be safely concluded that Ca exhibits stronger P affinity than Mg based on the above thermodynamic analysis.

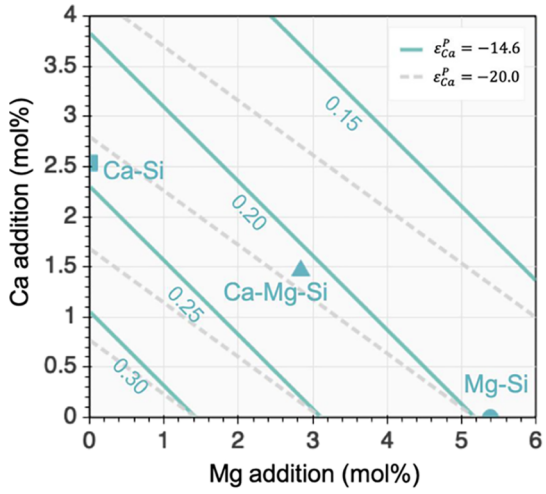

Figure 14. Calculated isocurves of the P segregation coefficient with varying Ca and Mg additions for different ε^P_{Ca} values; symbols show the experimental compositional locations of the studied alloys.

CONCLUSIONS

In the present work, a comparative study of MG-Si leaching purification with Mg, Ca, and Mg−Ca additions to MG-Si was carried out. The following conclusions were drawn:

- The doping metal significantly affects the alloy microstructure, leaching behavior, and Si purification efficiency.
- In the Ca−Si alloy, the main precipitate was $CaSi_2$ and it led to the formation of a viscous byproduct siloxene during acid leaching along with a strong cracking effect. This causes the fastest leaching kinetics and the highest impurity removal efficiency. However, this cracking effect lowered the Si recovery compared to other samples.
- The Mg−Si alloy system achieved the highest Si recovery with the highest impurity removal efficiency, especially P removal. Nevertheless, the main precipitate Mg_2Si led to the slowest leaching kinetics.
- In the Ca−Mg−Si alloy system, the main phase was determined as $Ca_7Mg_{7.5\pm\delta}Si_{14}$ with a unique crystal structure that contains both a planar Si_{12} ring and isolated Si. As a result, the leaching of the Ca−Mg−Si alloy was found to be a cleaner process that avoids the disadvantages of both Ca−Si and Mg−Si systems. In addition, high Si recovery remained with fast leaching kinetics and high impurity removal, especially P removal.
- A cracking−shrinking principle-based kinetics model was developed for the leaching kinetics of Mg−Si and Ca−Mg−Si alloys. Thermodynamic analysis further revealed that the P removal ability is related to the doping metal concentration and its interaction coefficient with P, while Ca shows a stronger affinity to P than that of Mg.
- The novel Ca−Mg−Si ternary alloy system exhibited more sustainable performance as compared to the other two binary alloys.

AUTHOR INFORMATION

Corresponding Authors

Mengyi Zhu − *Department of Materials Science and Engineering, Norwegian University of Science and Technology (NTNU), N-7491 Trondheim, Norway;* orcid.org/0000-0002-5758-9747; Email: mengyi.zhu@ntnu.no

Sheng Ying Yue − *Department of Mechanical Engineering, University of California, Santa Barbara, California 93106, United States; Aachen Institute for Advanced Study in Computational Engineering Science (AICES), RWTH Aachen University, Aachen 52062, Germany;* orcid.org/0000-0003-2646-579X; Email: sheng.ying.yue@rwth-aachen.de

Authors

Kai Tang − *SINTEF Industry, N-7491 Trondheim, Norway*

Jafar Safarian − *Department of Materials Science and Engineering, Norwegian University of Science and Technology (NTNU), N-7491 Trondheim, Norway*

Complete contact information is available at: https://pubs.acs.org/10.1021/acssuschemeng.0c05564

https://dx.doi.org/10.1021/acssuschemeng.0c05564
ACS Sustainable Chem. Eng. XXXX, XXX, XXX−XXX

Notes

The authors declare no competing financial interest.

■ ACKNOWLEDGMENTS

This work was performed at NTNU within the Research Center for Sustainable Solar Cell Technology (FME SuSolTech, project number 257639), co-sponsored by the Norwegian Research Council and industry partners.

■ REFERENCES

(1) Murgau, A.; Safarian, J. Solar Silicon Production through Metallurgical Route and REC Solar Advancements. *Silicon Chem. Sol. Ind. XIV* **2018**, 183−192.
(2) Safarian, J.; Tranell, G.; Tangstad, M. Processes for Upgrading Metallurgical Grade Silicon to Solar Grade Silicon. *Energy Procedia* **2012**, *20*, 88−97.
(3) Forniés, E.; Ceccaroli, B.; Méndez, L.; Souto, A.; Pérez Vázquez, A.; Vlasenko, T.; Dieguez, J. Mass Production Test of Solar Cells and Modules Made of 100% UMG Silicon. 20.76% Record Efficiency. *Energies* **2019**, *12*, 1495.
(4) Tucker, N. P. Preparation of High Purity Silicon. *J. Iron Steel Ind.* **1927**, *15*, 412−414.
(5) Dietl, J. Hydrometallurgical Purification of Metallurgical-Grade Silicon. *Sol. Cells* **1983**, *10*, 145−154.
(6) Chu, T. L.; Chu, S. S. Partial Purification of Metallurgical Silicon by Acid Extraction. *J. Electrochem. Soc.* **1983**, *130*, 455.
(7) Juneja, J. M.; Mukherjee, T. K. A Study of the Purification of Metallurgical Grade Silicon. *Hydrometallurgy* **1986**, *16*, 69−75.
(8) Santos, I. C.; Goncalves, A. P.; Santos, C. S.; Almeida, M.; Afonso, M. H.; Cruz, M. J. Purification of Metallurgical Grade Silicon by Acid Leaching. *Hydrometallurgy* **1990**, *23*, 237−246.
(9) Lu, H.; Wei, K.; Ma, W.; Xie, K.; Wu, J.; Lei, Y.; Dai, Y. Effect of Acetic Acid on the Leaching Behavior of Impurities in Metallurgical Grade Silicon. *Sep. Sci. Technol.* **2017**, *52*, 1257−1264.
(10) Guan, B.; Sun, Y.; Li, X.; Wang, J.; Chen, S.; Schweizer, S.; Wang, Y.; Wehrspohn, R. B. Conversion of Bulk Metallurgical Silicon into Photocatalytic Nanoparticles by Copper-Assisted Chemical Etching. *ACS Sustainable Chem. Eng.* **2016**, *4*, 6590−6599.
(11) Tian, C.; Lu, H.; Wei, K.; Ma, W.; Xie, K.; Wu, J.; Lei, Y.; Yang, B.; Morita, K. Effect of CH3COOH on Hydrometallurgical Purification of Metallurgical-Grade Silicon Using HCl-HF Leaching. *JOM* **2018**, *70*, 527−532.
(12) Liu, S.; Huang, K.; Zhu, H. Removal of Fe, B and P Impurities by Enhanced Separation Technique from Silicon-Rich Powder of the Multi-Wire Sawing Slurry. *Chem. Eng. J.* **2016**, *299*, 276−281.
(13) Zhao, D.; Li, Y. Revealing the Factors Influencing Grain Boundary Segregation of P, As in Si: Insights from First-Principles. *Acta Mater.* **2019**, *168*, 52−62.
(14) Anders, S.; Tuset, J. K.; Tveit, H. *Production of High Silicon Alloys*; Tapir Academic Press: Trondheim, Norway, 1998.
(15) Shimpo, T.; Yoshikawa, T.; Morita, K. Thermodynamic Study of the Effect of Calcium on Removal of Phosphorus from Silicon by Acid Leaching Treatment. *Metall. Mater. Trans. B* **2004**, *35*, 277−284.
(16) Lai, H.; Huang, L.; Lu, C.; Fang, M.; Ma, W.; Xing, P.; Li, J.; Luo, X. Leaching Behavior of Impurities in Ca-Alloyed Metallurgical Grade Silicon. *Hydrometallurgy* **2015**, *156*, 173−181.
(17) Johnston, M. D.; Barati, M. Calcium and Titanium as Impurity Getter Metals in Purification of Silicon. *Sep. Purif. Technol.* **2013**, *107*, 129−134.
(18) Meteleva-Fischer, Y. V.; Yang, Y.; Boom, R.; Kraaijveld, B.; Kuntzel, H. Microstructure of Metallurgical Grade Silicon and Its Acid Leaching Behaviour by Alloying with Calcium. *Miner. Process. Extr. Metall.* **2013**, *122*, 229−237.
(19) Espelien, S.; Safarian, J. Effect of Acid Leaching Conditions on Impurity Removal from Silicon Doped by Magnesium. *AIMS Energy* **2017**, *5*, 636−651.
(20) Safarian, J.; Espelien, S. In *Hydrometallurgical Purification of Maganesium-Doped Silicon by Difference Acids*, 33 European Photovoltaic Solar Energy Conference and Exhibition, 2017; pp 480−482.
(21) Zhu, M.; Murgau, A.; Safarian, J. In *Effects of Magnesium-Doping on Silicon Leaching for Solar Grade Feedstock Production*, 35 European Photovoltaic Solar Energy Conference and Exhibition, 2018; pp 465−468.
(22) Espelien, S.; Tranell, G.; Safarian, J. Effect of Magnesium Addition on Removal of Impurities from Silicon by Hydrometallurgical Treatment. In *Energy Technology 2017*; Springer, 2017; pp 355−366.
(23) Zhu, M.; Azarov, A.; Monakhov, E.; Tang, K.; Safarian, J. Phosphorus Separation from Metallurgical-Grade Silicon by Magnesium Alloying and Acid Leaching. *Sep. Purif. Technol.* **2020**, *240*, No. 116614.
(24) Yoshikawa, T.; Morita, K. Refining of Silicon during Its Solidification from a Si−Al Melt. *J. Cryst. Growth* **2009**, *311*, 776−779.
(25) Ban, B.; Bai, X.; Li, J.; Li, Y.; Chen, J.; Dai, S. The Mechanism of P Removal by Solvent Refining in Al-Si-P System. *Metall. Mater. Trans. B* **2015**, *46*, 2430−2437.
(26) Yoshikawa, T.; Morita, K. Removal of Phosphorus by the Solidification Refining with Si-Al Melts. *Sci. Technol. Adv. Mater.* **2003**, *4*, 531−537.
(27) Yu, W.; Ma, W.; Lv, G.; Ren, Y.; Dai, Y.; Morita, K. Low-Cost Process for Silicon Purification with Bubble Adsorption in Al-Si Melt. *Metall. Mater. Trans. B* **2014**, *45*, 1573−1578.
(28) Li, J.-W.; Zhan-Cheng, G.; Li, Li. J.-C.; Yu, Zhi. Super Gravity Separation of Purified Si from Solvent Refining with the Al-Si Alloy System for Solar Grade Silicon. *Silicon* **2015**, *7*, 239−246.
(29) Lei, Y.; Qiu, P.; Chen, K.; Chen, X.; Ma, W.; Wu, J.; Wei, K.; Li, S.; Lv, G.; Qiu, J. Mechanism of ZrB2 Formation in Al-Si Alloy and Application in Si Purification. *ACS Sustainable Chem. Eng.* **2019**, *7*, 12990−12996.
(30) Huang, L.; Lai, H.; Lu, C.; Fang, M.; Ma, W.; Xing, P.; Li, J.; Luo, X. Enhancement in Extraction of Boron and Phosphorus from Metallurgical Grade Silicon by Copper Alloying and Aqua Regia Leaching. *Hydrometallurgy* **2016**, *161*, 14−21.
(31) Ren, Y.; Ueda, S.; Morita, K. Formation Mechanism of ZrB2 in a Si-Cu Melt and Its Potential Application for Refining Si and Recycling Si Waste. *ACS Sustainable Chem. Eng.* **2019**, *7*, 20107−20113.
(32) Huang, L.; Danaei, A.; Thomas, S.; Xing, P.; Li, J.; Luo, X.; Barati, M. Solvent Extraction of Phosphorus from Si-Cu Refining System with Calcium Addition. *Sep. Purif. Technol.* **2018**, *204*, 205−212.
(33) Ren, Y.; Morita, K. Low-Temperature Process for the Fabrication of Low-Boron Content Bulk Si from Si−Cu Solution with Zr Addition. *ACS Sustainable Chem. Eng.* **2020**, *8*, 6853−6860.
(34) Li, Y.; Zhang, L. Application of Si-Based Solvents to the Purification of Metallurgical Grade-Silicon. *Sep. Purif. Rev.* **2019**, 1−24.
(35) Ma, X.; Lei, Y.; Yoshikawa, T.; Zhao, B.; Morita, K. Effect of Solidification Conditions on the Silicon Growth and Refining Using Si−Sn Melt. *J. Cryst. Growth* **2015**, *430*, 98−102.
(36) Khajavi, L. T.; Morita, K.; Yoshikawa, T.; Barati, M. Removal of Boron from Silicon by Solvent Refining Using Ferrosilicon Alloys. *Metall. Mater. Trans. B* **2015**, *46*, 615−620.
(37) Margarido, F.; Bastos, M. H.; Figueueiredo, M. O.; Martins, J. P. The Structural Effect on the Kinetics of Acid Leaching Refining of Fe-Si Alloys. *Mater. Chem. Phys.* **1994**, *38*, 342−347.
(38) Margarido, F.; Martins, J. P.; Figueueiredo, M. O.; Bastos, M. H. Kinetics of Acid Leaching Refining of an Industrial Fe-Si Alloy. *Hydrometallurgy* **1993**, *34*, 1−11.
(39) Yin, Z.; Oliazadeh, A.; Esfahani, S.; Johnston, M.; Barati, M. Solvent Refining of Silicon Using Nickel as Impurity Getter. *Can. Metall. Q.* **2011**, *50*, 166−172.
(40) Nesper, R. The Zintl-Klemm Concept - A Historical Survey. *Z. Anorg. Allg. Chem.* **2014**, *640*, 2639−2648.
(41) Kresse, G.; Furthmüller, J. Efficiency of Ab-Initio Total Energy Calculations for Metals and Semiconductors Using a Plane-Wave Basis Set. *Comput. Mater. Sci.* **1996**, *6*, 15−50.

https://dx.doi.org/10.1021/acssuschemeng.0c05564
ACS Sustainable Chem. Eng. XXXX, XXX, XXX−XXX

(42) Kresse, G.; Furthmüller, J. Efficient Iterative Schemes for Ab Initio Total-Energy Calculations Using a Plane-Wave Basis Set. *Phys. Rev. B* **1996**, *54*, 11169−11186.
(43) Blöchl, P. E. Projector Augmented-Wave Method. *Phys. Rev. B* **1994**, *50*, 17953−17979.
(44) Kresse, G.; Joubert, D. From Ultrasoft Pseudopotentials to the Projector Augmented-Wave Method. *Phys. Rev. B* **1999**, *59*, 1758−1775.
(45) Perdew, J. P.; Burke, K.; Ernzerhof, M. Generalized Gradient Approximation Made Simple. *Phys. Rev. Lett.* **1996**, *77*, 3865−3868.
(46) Klimeš, J.; Bowler, D. R.; Michaelides, A. Chemical Accuracy for the van Der Waals Density Functional. *J. Phys.: Condens. Matter* **2010**, *22*, No. 022201.
(47) Klime, J.; Bowler, D. R.; Michaelides, A. Van Der Waals Density Functionals Applied to Solids. *Phys. Rev. B* **2011**, *83*, No. 195131.
(48) Bellaiche, L.; Vanderbilt, D. Virtual Crystal Approximation Revisited: Application to Dielectric and Piezoelectric Properties of Perovskites. *Phys. Rev. B* **2000**, *61*, 7877−7882.
(49) Miedema, A. R.; de Châtel, P. F.; de Boer, F. R. Cohesion in Alloys - Fundamentals of a Semi-Empirical Model. *Physica B+C* **1980**, *100*, 1−28.
(50) Takeuchi, A.; Inoue, A. Classification of Bulk Metallic Glasses By Atomic Size Difference, Heat of Mixing and Period of Constituent Elements and Its Application To Characterization of the Main Alloying Element. *Mater. Trans.* **2005**, *46*, 2817−2829.
(51) Gröbner, J.; Chumak, I.; Schmid-Fetzer, R. Experimental Study of Ternary Ca−Mg−Si Phase Equilibria and Thermodynamic Assessment of Ca−Si and Ca−Mg−Si Systems. *Intermetallics* **2003**, *11*, 1065−1074.
(52) Villars, P.; Cenzual, K.; Daams, J.; Gladyshevskii, R.; Shcherban, O.; Dubenskyy, V.; Melnichenko-Koblyuk, N.; Pavlyuk, O.; Stoiko, S.; Sysa, L. *Landolt-Börnstein New Series III/43A3*, 2006.
(53) Nesper, R.; Currao, A.; Wengert, S. Nonaromatic Planar Si12 Ring System of Approximate D(6h) Symmetry in Ca7Mg(7.5±δ)Si14. *Chem. - Eur. J.* **1998**, *4*, 2251−2257.
(54) Uehara, M.; Katagiri, A.; Kurokawa, M.; Akiyama, K.; Shimizu, T.; Matsushima, M.; Uchida, H.; Kimura, Y.; Funakubo, H. Preparation of CaMgSi and Ca7Mg7.25Si14 Single Phase Films and Their Thermoelectric Properties. *MRS Adv.* **2019**, *4*, 1503−1508.
(55) Cui, S.; Paliwal, M.; Jung, I.-H. Thermodynamic Optimization of Ca-Fe-Si System and Its Applications to Metallurgical Grade Si-Refining Process. *Metall. Mater. Trans. E* **2014**, *1*, 67−79.
(56) Margaria, T.; Anglezio, J.; Servant, C. In *Inlcrmetallic Compounds in Metallurgical Silicon*, Proceedings of the 6th International Ferroalloys Congress, Cape Town, 1992; pp 209−214.
(57) Vogg, G.; Brandt, M. S.; Stutzmann, M. Kinetics of the Topotactic Formation of Siloxene. *Chem. Mater.* **2003**, *15*, 910−915.
(58) Stutzmann, M.; Brandt, M. S.; Rosenbauer, M.; Fuchs, H. D.; Finkbeiner, S.; Weber, J.; Deak, P. Luminescence and Optical Properties of Siloxene. *J. Lumin.* **1993**, *57*, 321−330.
(59) Baranek, P.; Schamps, J.; Noiret, I. Ab Initio Studies of Electronic Structure, Phonon Modes, and Elastic Properties of Mg2Si. *J. Phys. Chem. B* **1997**, *101*, 9147−9152.
(60) Nandi, K. C.; Mukherjee, D.; Biswas, A. K.; Acharya, H. N. Optimization of acid concentration, temperature and particle size of magnesium silicide, obtained from rice husk, for the production of silanes. *J. Mater. Sci. Lett.* **1993**, *12*, 1248−1250.
(61) Vijh, A. K.; Bélanger, G. Some Trends in the Electrocatalytic Activities of Metal Silicides for the Hydrogen Evolution Reaction. *J. Mater. Sci. Lett.* **1995**, *14*, 982−984.
(62) Martins, J. P.; Margarido, F. The Cracking Shrinking Model for Solid-Fluid Reactions. *Mater. Chem. Phys.* **1996**, *44*, 156−169.
(63) Fang, M.; Lu, C.; Huang, L.; Lai, H.; Chen, J.; Li, J.; Ma, W.; Xing, P.; Luo, X. Effect of Calcium-Based Slag Treatment on Hydrometallurgical Purification of Metallurgical-Grade Silicon. *Ind. Eng. Chem. Res.* **2014**, *53*, 972−979.
(64) Martins, J. P.; Margarido, F. The Cracking Shrinking Model for Solid-Fluid Reactions. *Mater. Chem. Phys.* **1996**, *44*, 156−169.
(65) Dickinson, C. F.; Heal, G. R. A Review of the ICTAC Kinetics Project, 2000. Part 1. Isothermal Results. *Thermochim. Acta* **2009**, *494*, 1−14.
(66) Kröger, C.; Ziegler, G. Über Die Geschwindigkeiten Der Zur Glasschmelze Führenden Reaktionen. III. *Glas. Berichte* **1954**, *27*, 199−212.
(67) Kröger, C.; Ziegler, G. Über Die Geschwindigkeiten Der Zur Glasschmelze Führenden Reaktionen. II. *Glas. Berichte* **1953**, *26*, 346−353.
(68) Jander, W. Reaktionen Im Festen Zustande Bei Höheren Temperaturen. Säureplatzwechsel Bei Einigen Wolframaten Und Molybdaten. *Z. Anorg. Allg. Chem.* **1930**, *190*, 397−406.
(69) Provis, J. L. On the Use of the Jander Equation in Cement Hydration Modeling. *RILEM Tech. Lett.* **2016**, *1*, 62.
(70) Khawam, A.; Flanagan, D. R. Solid-State Kinetic Models: Basics and Mathematical Fundamentals. *J. Phys. Chem. B* **2006**, *110*, 17315−17328.
(71) Ginstling, A.; Brounshtein, B. I. Concerning the Diffusion Kinetics of Reactions in Spherical Particles. *J. Appl. Chem. USSR* **1950**, *23*, 1327−1338.
(72) Bale, C. W.; Pelton, A. D. The Unified Interaction Parameter Formalism: Thermodynamic Consistency and Applications. *Metall. Mater. Trans. A* **1990**, *21*, 1997−2002.

https://dx.doi.org/10.1021/acssuschemeng.0c05564
ACS Sustainable Chem. Eng. XXXX, XXX, XXX−XXX